







# Moisture adsorption by decellularized bovine pericardium collagen matrices studied by terahertz pulsed spectroscopy and solid immersion microscopy

G. R. MUSINA,<sup>1,2,9</sup> N. V. CHERNOMYRDIN,<sup>1,3,4</sup> E. R. GAFAROVA,<sup>3,4</sup>  
A. A. GAVDUSH,<sup>1,2</sup> A. J. SHPICHKA,<sup>3,4,5</sup> G. A. KOMANDIN,<sup>1,2</sup>  V.  
B. ANZIN,<sup>1</sup> E. A. GREBENIK,<sup>3</sup> M. V. KRAVCHIK,<sup>6</sup>  E. V.  
ISTRANOVA,<sup>3</sup> I. N. DOLGANOVA,<sup>3,4,7</sup>  K. I. ZAYTSEV,<sup>1,2,3,10</sup>  AND  
P. S. TIMASHEV<sup>3,4,5,8,11</sup>

<sup>1</sup>Prokhorov General Physics Institute of the Russian Academy of Sciences, Russia

<sup>2</sup>Bauman Moscow State Technical University, Russia

<sup>3</sup>Institute for Regenerative Medicine, Sechenov First Moscow State Medical University (Sechenov University), Russia

<sup>4</sup>World-Class Research Center “Digital Biodesign & Personalized Healthcare”, Sechenov First Moscow State Medical University (Sechenov University), Russia

<sup>5</sup>Chemistry Department, Lomonosov Moscow State University, Russia

<sup>6</sup>Scientific Research Institute of Eye Diseases, Russia

<sup>7</sup>Institute of Solid State Physics of the Russian Academy of Sciences, Russia

<sup>8</sup>Department of Polymers and Composites, N. N. Semenov Institute of Chemical Physics, Russia

<sup>9</sup>guzel-musina12@mail.ru

<sup>10</sup>kirzay@gmail.com

<sup>11</sup>timashev\_p\_s@staff.sechenov.ru

**Abstract:** In this paper, terahertz (THz) pulsed spectroscopy and solid immersion microscopy were applied to study interactions between water vapor and tissue scaffolds—the decellularized bovine pericardium (DBP) collagen matrices, in intact form, cross-linked with the glutaraldehyde or treated by plasma. The water-absorbing properties of biomaterials are prognostic for future cell-mediated reactions of the recipient tissue with the scaffold. Complex dielectric permittivity of DBPs was measured in the 0.4–2.0 THz frequency range, while the samples were first dehydrated and then exposed to water vapor atmosphere with  $80.0 \pm 5.0\%$  relative humidity. These THz dielectric measurements of DBPs and the results of their weighting allowed to estimate the adsorption time constants, an increase of tissue mass, as well as dispersion of these parameters. During the adsorption process, changes in the DBPs’ dielectric permittivity feature an exponential character, with the typical time constant of  $\approx 8\text{--}10$  min, the transient process saturation at  $\approx 30$  min, and the tissue mass improvement by  $\approx 1\text{--}3\%$ . No statistically-relevant differences between the measured properties of the intact and treated DBPs were observed. Then, contact angles of wettability were measured for the considered DBPs using a recumbent drop method, while the observed results showed that treatments of DBP somewhat affects their surface energies, polarity, and hydrophilicity. Thus, our studies revealed that glutaraldehyde and plasma treatment overall impact the DBP–water interactions, but the resultant effects appear to be quite complex and comparable to the natural variability of the tissue properties. Such a variability was attributed to the natural heterogeneity of tissues, which was confirmed by the THz microscopy data. Our findings are important for further optimization of the scaffolds’ preparation and treatment technologies. They pave the way for THz technology use as a non-invasive diagnosis tool in tissue engineering and regenerative medicine.

© 2021 Optical Society of America under the terms of the [OSA Open Access Publishing Agreement](#)

## 1. Introduction

The scaffold – water interactions, including the water adsorption by scaffold, are of great importance in tissue engineering and regenerative medicine. The water adsorption might have both adverse and beneficial effects on the scaffold behavior. On the one hand, water adsorption is a valuable property, that provides the hydrolytic degradation of scaffolds and the nutrients transport [1]. On the other hand, it can negatively impact the mechanical properties of scaffolds, along with the cell proliferation and structural morphology of the regenerated tissue [2,3]. Thereby, an increasing demand for a detailed study and description of the scaffold hydration and dehydration kinetics under various conditions is observed.

Terahertz (THz) technology forms a perspective tool for solving this challenging problem, thanks to the advanced sensitivity of THz waves to the content and state (free or bound) of tissue water [4–9]. Indeed, with a rapid progress in THz emitters, detectors and optical components during the past few decades [10–18], such techniques as THz spectroscopy, imaging, reflectometry, and others were applied in oncodiagnosis [19–25], sensing of tissue hydration [26,27], determining the degree of traumatic tissue injuries [28,29] and burns [30], diagnosis of glycated tissues and diabetes mellitus [31–33], and evaluation of transdermal drug delivery [34], while all these biomedical applications rely mostly on tissue water, as an endogenous label of pathological process. Nevertheless, applications of THz technology in tissue engineering and regenerative medicine and, particularly, in studying the scaffold – water interactions still remain unaddressed.

Previously, fundamental aspects of the electromagnetic-wave interactions with tissue matrices of different kind were studied in several research articles. Particularly, in Ref. [35], Motovilov et al. measured and analyzed the broadband dielectric response of the *Shewanella oneidensis* MR-1 extracellular matrix, along with its biochemical components, such as cytochrome C and serum albumin. They revealed many biophysical and metabolic features, that underlie the broadband dielectric permittivity of this object. In Ref. [36], the *Shewanella oneidensis* MR-1 extracellular matrix, cytochrome C, and serum albumin were measured in a broad spectral range (including the THz band), with a focus on the contribution of tissue water under different temperature conditions. In few more Refs. [37–39], various biological and biochemical features of cellular matrices, cellular and intercellular components were investigated involving the THz spectroscopy. At the same time, applied aspects of the THz-wave interactions with decellularized tissues, prepared specifically to address challenges of the tissue engineering and regenerative medicine, have not been considered yet, to the best of our knowledge.

In this paper, interactions between tissue scaffolds and water vapor are studied, involving both the diffraction-limited THz pulsed spectroscopy (TPS) and the sub-wavelength-resolution THz solid immersion microscopy (SIM). Intact, cross-linked by GlutarAldehyde (GA) and treated by plasma decellularized bovine pericardium (DBP) are considered. Relying on the TPS data, complex dielectric permittivity of these scaffolds is estimated at the frequencies of 0.4–2.0 THz, when the samples are dehydrated (dried in vacuum) and, then, exposed to water vapor at the relative humidity of  $80.0 \pm 5.0\%$ . Thus, studied dielectric response of DBPs, along with their weighting measurements, yields estimations of the adsorption process parameters. A simple exponential model accurately described all changes in the THz dielectric response function for all the considered DBP types, with the typical time constant of  $\tau \approx 8\text{--}10$  min, the transient process saturation at  $\approx 30$  min, and tissue mass increase by  $\Delta m \approx 1\text{--}3\%$ . Then, contact angles of wettability are measured for the considered DBPs using a recumbent drop method. The results of these measurements indicated that treatments of DBP somewhat affect their surface energies, polarity, and hydrophilicity. Our findings revealed that GA and plasma treatment overall impact the DBP – water interactions. At the same time, the resultant effects are quite complex and comparable to the natural tissue variability. Such variability was attributed to

the natural heterogeneity of tissues, that is confirmed for the considered DBP types using the 0.15  $\lambda$ -resolution THz SIM system.

## 2. Materials and methods

### 2.1. Preparation of the DBP samples

The work with animals was carried out in accordance with the ethical principles established by the European Convention for the Protection of Vertebrate Animals used for Experimental and Other Scientific Purposes (Strasbourg, 2006) and the International Guidelines for Biomedical Research in Animals (CIOMS and ICLAS, 2012). Pericardium tissues from young calves were obtained directly from a local slaughterhouse and transported to our laboratory in a cold hypertonic solution. The excess fat and connective tissue were carefully removed from tissue specimens.

Decellularization was achieved by the treatment of tissues in a mixture of 1 M sodium hydroxide and 0.85 M sodium sulfate for 2 hours at the temperature of 20°C followed by rinsing with water and neutralization with 4% (wt/v) boric acid for 1 hour. Finally, decellularized tissue was thoroughly rinsed with water and then freeze-dried. Thus obtained DBP samples with the thicknesses in the range of  $l = 0.54\text{--}0.74$  mm were cut into fragments with the surface area of  $22 \times 13$  mm<sup>2</sup> and, then, divided into three groups for further experimental studies:

- Intact DBP collagen matrices; see Fig. 1(a),(b).
- Those cross-linked with GA. For this aim, 3 ml of GA was added to the bottom of the desiccator with a scaffold, covered with filter paper to form a tanning chamber, and kept, for 7 hours, until yellowing; see Fig. 1(c),(d).
- Those treated by plasma. For this aim, a scaffold was processed, for 60 sec, with a synthetic air and low-frequency burst at the power of 50 W, the frequency of 40 kHz, and the pressure of 66.6 Pa; see Fig. 1(e),(f).

In this way, we obtain a number of DBP samples from each group for the further THz spectroscopy, microscopy, measurements of weight and contact angles.

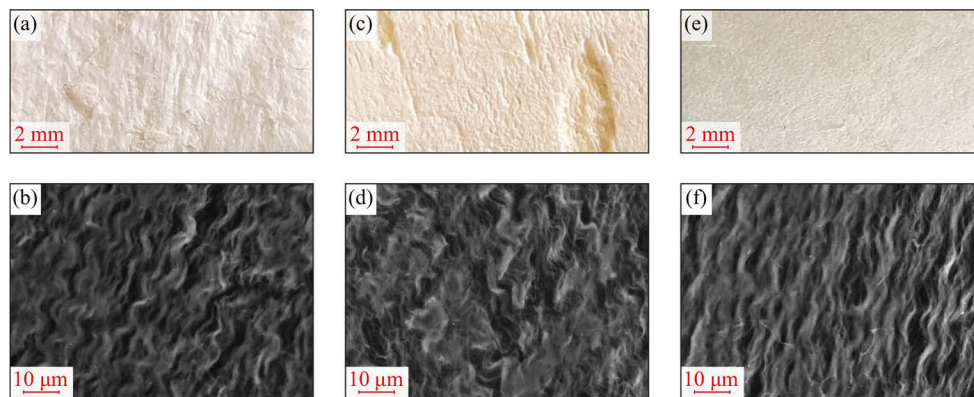


**Fig. 1.** Visible photos (top row) and scanning electron microscopy images (bottom row), collected by the Zeiss EVO LS10 system (Germany), of the studied DBP collagen matrices. (a),(b) Intact. (c),(d) Cross-linked with GA. (e),(f) Treated by plasma.

### 2.2. In-house TPS setup

For the THz spectroscopy of DBPs, an in-house TPS setup was used [40]. In Figs. 2(a) and (b), a scheme and a photo of this setup are shown. It relies on photoconductive antennas [11,13], as

both an emitter and a detector of THz pulses, operates in the transmission mode, and is equipped with a vacuum THz beam path and a vacuum sample chamber, that are aimed at suppressing an impact of water vapors on the measured THz data. The pressure in both vacuum chambers was measured using a Thyracont VD85 vacuum meter with a piezo / Pirani combination sensor featuring the accuracy of 10%. Our TPS yields measurements of the DBP collagen matrices in the frequency range of 0.4–2.0 THz with the spectral resolution as high as 0.015 THz. It uses a focused THz beam, which makes possible measuring sample with the diameters of  $\geq 4$  mm, with minimal distortions of a measured spectra due to diffraction phenomenon. At the same time, the THz beam aperture is small enough, thus, the plane wave approximation can be applied to model the THz-wave – sample interactions and to resolve the TPS inverse problems. For more details of the TPS design and operation, see Refs. [41–43].

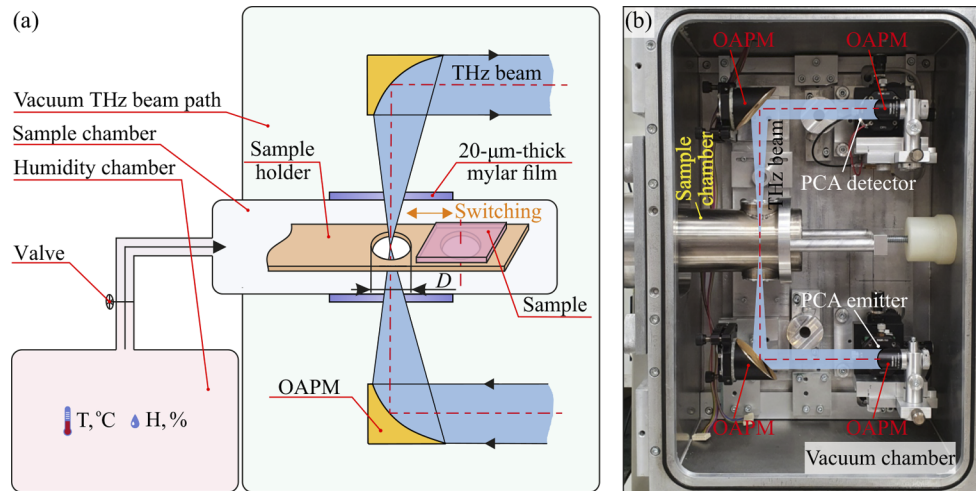


**Fig. 2.** (a) A scheme and (b) a photo of the in-house TPS setup assembled to study the THz dielectric response of the DBP collagen matrices during their exposure to water vapor. Here, PCA stands for a photoconductive antenna; OAPM is an off-axis parabolic mirror. In this setup, switching between reference and sample diaphragms inside the sample chamber yields measuring the reference  $E_r$  and sample  $E_s$  TPS waveforms.

The sample is handled in a special chamber, that is, first, vacuumized to study the dehydrated tissues. Then, this chamber is purged with water vapor to study kinetics of its adsorption by tissues. To separate the vacuum THz beam path and the sample chamber, a 20- $\mu$ m-thick mylar film is used, being optically transparent in the THz range and thick enough to avoid THz standing waves and related modulations in THz spectra. The measured tissue are placed atop of the sample holder, that can be translated transverse to the optical axis in order to switch between the equal  $D = 5$  mm-diameter reference and sample diaphragms. During measurements, a DBP tissue completely closes the sample diaphragm, while the reference diaphragm remains empty.

For the sample purging with water vapor, a separate humidity chamber with the volume of  $\approx 0.08$  m<sup>3</sup> is used. It allows us to prepare a water vapor atmosphere with the stabilized temperature of  $\approx 25^\circ\text{C}$  and the desired relative humidity of  $80.0 \pm 5.0\%$ . For this aim, a judiciously-designed camera, a humidifier, and a precise thermohygrometer Testo 635 (Germany) with the accuracy of humidity and temperature measurements of 0.1% and 0.1 $^\circ\text{C}$ , respectively, are used. This atmosphere is introduced into the vacuumized sample chamber by opening a valve. The humidity chamber volume is much larger than that of a sample chamber, thus, the atmosphere in these two volumes is assumed to be equal to that in a separately-operating humidity chamber after opening the valve.

The measurement procedure includes the following main steps:

- (1) A DBP sample is placed atop of the sample holder to close the sample aperture.
- (2) The THz beam path and the sample chamber are vacuumized, while the valve between the sample and humidity chambers is closed.
- (3) A DBP sample is dried for  $\approx 1$  hour in the sample chamber at a residual pressure of  $<10^{-1}$  mbar.
- (4) Reference  $E_r$  and sample  $E_s$  TPS waveforms are measured for this dehydrated DBP sample by switching the position of sample holder.
- (5) The valve between the sample and humidity chambers is opened, thus, introducing the moisture into the sample chamber and starting the adsorption process.
- (6) Then, reference  $E_r$  and sample  $E_s$  TPS waveforms are continuously measured during the water adsorption by a DBP sample with the time intervals of 2 min, until saturation.

### 2.3. TPS-based estimation of the DBP optical properties

For the physically-reasonable analysis of the TPS data, we estimate the THz complex dielectric permittivity  $\tilde{\varepsilon}$  of both the dehydrated DBP samples and those exposed to water vapor

$$\tilde{\varepsilon} = \varepsilon' - i\varepsilon'', \quad (1)$$

with its real  $\varepsilon'$  and imaginary  $\varepsilon''$  parts. For this aim, we apply a procedure from Refs. [43,44]. For dehydrated DBPs and for each of their hydration state, it implies detection of both the reference  $E_r(t)$  and sample  $E_s(t)$  waveforms, as illustrated in Fig. 3. The reference signal corresponds to the THz pulse passed through the empty diaphragm, while the sample one – through the diaphragm closed by a measured tissue.

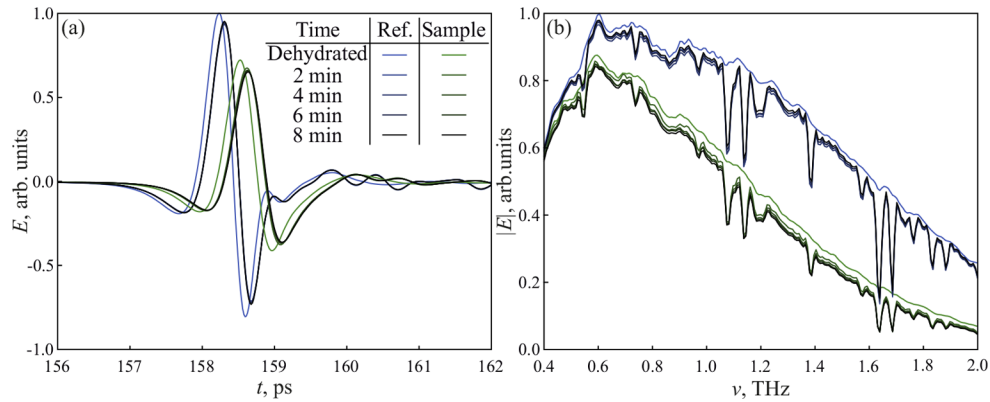


**Fig. 3.** Examples of (a) the reference  $E_r(t)$  and sample  $E_s(t)$  time-domain TPS waveforms and (b) their Fourier spectra  $E_r(\nu)$  and  $E_s(\nu)$ , which correspond to a representative 0.55-mm-thick dehydrated intact DBP collagen matrix, as well as that exposed to water vapor for 2–8 min.



Complex dielectric permittivity of tissues is estimated by minimization of an error functional – i.e., a discrepancy between experimental data and a theoretical model:

$$\tilde{\varepsilon} = \operatorname{argmin}_{\tilde{\varepsilon}} [\Phi], \quad \Phi = \left( \begin{array}{l} |H_{\text{exp}}| - |H_{\text{th}}(\nu)| \\ \phi[H_{\text{exp}}] - \phi[H_{\text{th}}(\nu)] \end{array} \right), \quad (2)$$

where  $H_{\text{exp}}, H_{\text{th}}$  are frequency-dependent experimental and theoretical transfer functions, and  $|\dots|, \phi[\dots]$  stand for the modulus and phase operators, respectively. The function  $H_{\text{exp}}$  is calculated based on the measured TPS waveforms

$$H_{\text{exp}} = \frac{E_s(\nu)}{E_r(\nu)} = \frac{\mathcal{F}_t[E_s(t)]}{\mathcal{F}_t[E_r(t)]}, \quad (3)$$

where  $\mathcal{F}_t[\dots]$  is the direct Fourier transform operator. In turn, the function  $H_{\text{th}}$  is defined analytically as

$$H_{\text{th}} = T_{0,1} T_{1,0} \frac{P_1(l_1)}{P_0(l_1)} \sum_{j=0}^N (P_1(l_1) R_{1,0})^{2j}, \quad (4)$$

considering the finite number  $N$  of the THz-wave resonances and, thus, the related standing waves inside the measured tissue specimen.

In Eq. (4), a modified Bouguer-Lambert-Beer law is used to describe attenuation and phase delay of the THz-wave propagating through a bulk medium with the complex refractive index  $\tilde{n} = \sqrt{\tilde{\varepsilon}}$  over the length  $l$

$$P(\tilde{\varepsilon}, l) = \exp\left(-i \frac{2\pi\nu}{c_0} \sqrt{\tilde{\varepsilon}} l\right), \quad (5)$$

where  $c_0 \approx 3 \times 10^8$  m/s is the speed of light in free space, and  $\nu$  is an electromagnetic-wave frequency. In turn, the Fresnel formulas (for the normal incidence) are used to define the THz-wave reflection and transmission (by amplitude) at the interface between the two media –  $m$  and  $k$ :

$$R_{m,k} = \frac{\sqrt{\tilde{\varepsilon}_m} - \sqrt{\tilde{\varepsilon}_k}}{\sqrt{\tilde{\varepsilon}_m} + \sqrt{\tilde{\varepsilon}_k}}, \quad T_{m,k} = \frac{2\sqrt{\tilde{\varepsilon}_m}}{\sqrt{\tilde{\varepsilon}_m} + \sqrt{\tilde{\varepsilon}_k}}, \quad (6)$$

with their complex refractive indices  $\tilde{n}_m = \sqrt{\tilde{\varepsilon}_m}$  and  $\tilde{n}_k = \sqrt{\tilde{\varepsilon}_k}$ .

In Fig. 4, representative examples of the measured complex dielectric permittivity are shown, with an increasing duration of DBP exposure to water vapor: panels (a),(b) correspond to an intact DBP sample; (c),(d) – treated by GA, and (e),(f) – treated by plasma. Despite the dielectric data were collected during the total 1-hour-length exposure with the time step of 2 min, the observed changes in  $\tilde{\varepsilon}$  occur much slower, and such a small time step is a kind of oversampling. Therefore, in Fig. 4, the curves  $\varepsilon'$  and  $\varepsilon''$  are plotted with somewhat smaller time step, that makes possible readily analyzing the data and revealing pronounced changes in the THz dielectric response of DBPs.

## 2.4. TPS-based estimation of the water vapor adsorption parameters

### 2.4.1. Adsorption time constant

Assuming that the adsorption of water vapor by tissue scaffolds has a single time scale, adsorption time constant  $\tau$  is determined independently for each of the studied DBP samples using an approach from Ref. [45]. It implies analysis of the transient process observed in the measured TPS signals (either in time or frequency domains) during the adsorption process. For this aim, we normalize and average, over the considered 0.4–2.0 THz range, the time-dependent real dielectric

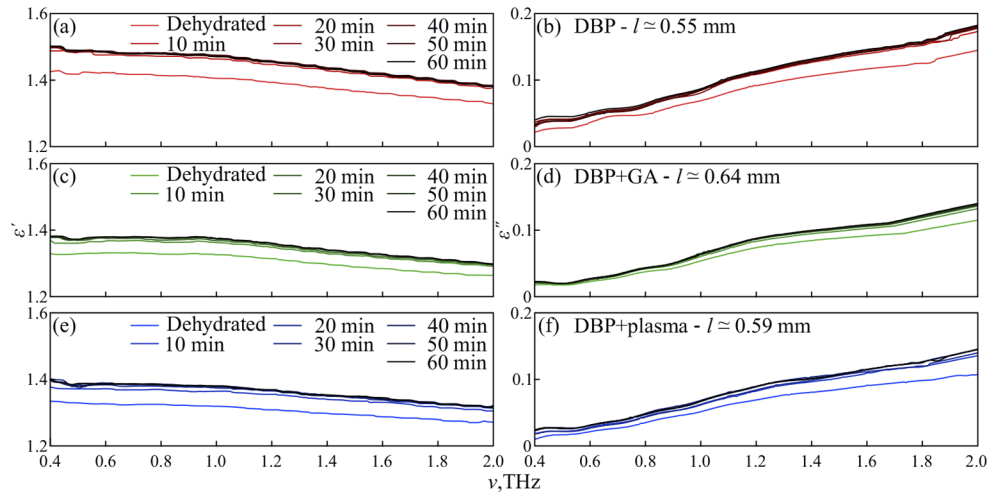


**Fig. 4.** Evolution of the THz dielectric permittivity of the DBP collagen matrices during their 1-hour-long exposure to water vapor at the relative humidity of  $80 \pm 5\%$ . (a),(b) Real  $\epsilon'$  and imaginary  $\epsilon''$  dielectric permittivity of a representative intact DBP sample. (c),(d) and (e),(f) Equal data for representative GA-treated (DBP+GA) and plasma-treated (DBP+plasma) samples, respectively.

permittivity  $\epsilon'(\nu, t)$ , aimed at improving the signal-to-noise ratio in thus calculated data. Then, we parametrize the function  $\langle \epsilon'(t) - 1 \rangle_\nu$  by the following transient process model

$$f(t) \propto 1 - \exp\left(-\frac{t}{\tau}\right), \quad (7)$$

using the weighted non-linear least square method, with the resultant time constant  $\tau$ .

In Fig. 5, estimation of the time constant  $\tau$  is illustrated for three different DBP samples – intact, cross linked by GA, and treated by plasma. Generally, tissue scaffolds possess quite high porosity and, thus, form complex highly-developed surface. For such complex object, adsorption, diffusion, and capillary flow processes can possess multiple time scales, governed by several times, or some continuous distribution of relaxation times, or even completely other non-exponential regularities; for example, see Ref. [20,46–48]. Moreover, when dealing with solutions of biological molecules and tissues, we can expect a complex non-linear relation between the dielectric permittivity and the content of tissue water due to hydration of biological molecules [6,49]. Nevertheless, from Fig. 5, we notice that even the considered simplest model accurately describes our experimental observations, while the transient process saturates after  $\approx 30$  min with no pronounce difference between the considered DBPs.

#### 2.4.2. Qualitative number of adsorbed water molecules

Next, relying on the TPS data, we estimate qualitatively the number  $N$  of adsorbed water molecules per unitary DBP volume. For this aim, we used the sum rule [8,50], from which it follows that the number of charges/dipoles underlying the dielectric response of a medium is proportional to the frequency-domain integral of its dynamic conductivity

$$N \propto \int_0^\infty \omega \epsilon'' d\omega = \text{finite}, \quad (8)$$

where  $\omega = 2\pi\nu$  is an angular frequency. Considering only the additive part of the dynamic conductivity, appeared as a result of water vapour adsorption, a robust estimation of the adsorbed

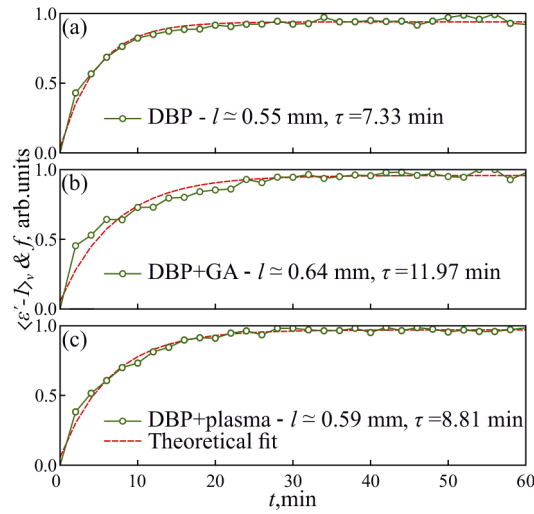


**Fig. 5.** Estimation of the adsorption time constant  $\tau$  of the DBP collagen matrices by fitting the time-dependent dielectric permittivity with the theoretical model (see Eq. (7)). (a) A comparison of the experimentally measured function  $\langle \epsilon'(t) - 1 \rangle_v$  (normalized and averaged within the considered spectral range) and theoretical fit  $f(t)$  for a representative intact DBP sample. (b),(c) Equal data for representative GA-treated (DBP+GA) and plasma-treated (DBP+plasma) samples, respectively.

water dipoles  $N$  (per unit volume) has the form

$$N \propto \int_{\omega_{\min}}^{\omega_{\max}} \omega \left( \epsilon''_{\text{moistured}} - \epsilon''_{\text{dehydrated}} \right) d\omega, \quad (9)$$

where  $\epsilon''_{\text{dehydrated}}$  and  $\epsilon''_{\text{moistured}}$  are imaginary parts of the DBP dynamic conductivity in the initial dehydrated state and after the adsorption process saturation.

It is worth noting that the described approach is quite approximate. Indeed, on the one hand, the integration is performed only within the finite  $[\omega_{\min}, \omega_{\max}]$  range of the TPS operation, but not over the all positive frequencies  $[0, \infty]$  or even over the range, in which water molecules contribute strongly to the tissue dynamic conductivity. On the other hand, it can be assumed that the dynamics of tissue water and, thus, the character (spectral shape) of its frequency-dependent dielectric response does not change notably with an increase of its content in tissues. Despite these assumptions, the method given by Eq. (9) leads to somewhat physically-reasonable estimations of tissue water content, as shown in Ref. [8].

### 2.5. Weighting of the DBP samples

Water adsorption by DBPs was also studied using a common weighting approach. For this aim, the DBP samples were, first, dehydrated in a vacuum chamber for 1 hour. Then, an analytical laboratory balance AND HR-250AZG, with the maximal mass limit of 210 mg and the resolution of 0.1 mg, was used to measure their mass  $m_{\text{dehydrated}}$ . Finally, all samples were weighed again after their exposure during 1 hour to water vapor with the relative humidity of  $80 \pm 5\%$  (the exposure conditions were the same as in the TPS experiments), with a resultant moistured sample mass  $m_{\text{moistured}}$ . In this way, an increment in the sample mass  $\Delta m$  was inferred

$$\Delta m = \frac{m_{\text{moistured}} - m_{\text{dehydrated}}}{m_{\text{dehydrated}}}. \quad (10)$$



## 2.6. Contact angles of the DBP samples

The surface properties of DBP samples were evaluated by measuring contact angles of wettability by the recumbent drop method using the Apex Instruments Acam-MS01 (India). Distilled water and pure Ethylene Glycol (EG) were used as test liquids. The measurements were carried out in atmosphere with the stabilized temperature of  $\approx 25^\circ\text{C}$  and the desired humidity of  $70.0 \pm 5.0\%$ . The contact angle of wettability values were determined as the average value of three measurements carried out on different areas of the collagen matrices after the droplet set. The Owens-Wendt-Rabel-Kaelble method was used to calculate the free surface energy. Within the framework of this method, the relationship between the components of the surface energy ( $\sigma^p$  – polar and  $\sigma^d$  – dispersion) and the contact angle of wettability  $\gamma$  is defined as

$$\frac{\sigma_l (1 + \cos(\gamma))}{2\sqrt{\sigma_l^d}} = \sqrt{\frac{\sigma_s^p \sigma_l^p}{\sigma_l^d}} + \sqrt{\sigma_s^d}, \quad (11)$$

where indices l, s indicate that the characteristic refers to a liquid or a solid, respectively.

## 2.7. In-house THz SIM setup

To study structural inhomogeneities of biological tissues and related inhomogeneous adsorption of water vapor, we use the sub-wavelength-resolution THz SIM imaging in the reflection-mode continuous-wave regime at the free-space wavelength of  $\lambda = 500 \mu\text{m}$  ( $\nu \approx 0.6 \text{ THz}$ ). This original modality of THz imaging was developed in Refs. [51–54]. It exploits the solid immersion effect – namely, a reduction in the THz-beam caustic (focal spot) dimensions, when it is formed in a free space (or in a low-refractive-index object), at a small distance ( $\ll \lambda$ ) behind a high-refractive-index material, with a contribution of both the propagating waves and the evanescent waves of the Total Internal Reflection (TIR) effect. By using the High-Resistivity Float-Zone Silicon (HRFZ-Si) [55], as such a high-refractive-index material ( $n_{\text{Si}} \approx 3.415$ ), our THz SIM overcomes the  $\sim 0.5\lambda$  Abbe diffraction limit of the electromagnetic-wave focusing in free space. It is capable of providing the advanced resolution, which depends slightly on the optical properties of an imaged object (as of any other modality of near-field imaging), but always remains strongly sub-wavelength – i.e., in the range of  $0.15\text{--}0.4\lambda$  [54].

The THz SIM system uses a backward-wave oscillator, as a continuous-wave THz emitter, and a Golay cell, as a THz beam power detector [51–54]. In Fig. 6, a key element of our THz SIM system is shown – namely, a solid immersion lens, that comprises the rigidly-fixed wide aperture aspherical singlet made of the High-Density PolyEthylene (HDPE), the rigidly-fixed HRFZ-Si hypohemisphere, and the movable HRFZ-Si window. Flat surfaces of the hypohemisphere and window are kept in close contact during the tissue imaging by its raster-scanning with a focused THz beam; thus, they form a unitary optical element – a solid immersion HRFZ-Si hemisphere, that serves as a resolution enhancer. The tissue is handled at the shadow side of this hemisphere and probed by both the propagating (ordinary-reflected) and evanescent waves. The imaging is performed by moving the HRFZ-Si window in the lateral directions (i.e., transverse to the optical axis). The spatial step of the 2D raster scanning system is set to  $\leq 0.075\lambda$ , aimed at satisfying the Whittaker–Nyquist–Kotelnikov–Shannon sampling theorem.

## 2.8. THz-SIM-based estimation of the DBP dielectric permittivity

As a result of THz SIM imaging, we detect a spatial distribution of THz-wave intensity  $I(\mathbf{r})$ , back-scattered from a solid immersion lens with or without an imaged object ( $\mathbf{r}$  is a radius vector at the object plane). These images  $I(\mathbf{r})$  are processed, aimed at resolving the THz SIM microscopy inverse problem – i.e., at estimation of the dielectric permittivity spatial distribution  $\varepsilon'(\mathbf{r})$  over the object plane. For this aim, we use a method from Ref. [56]. Since our THz

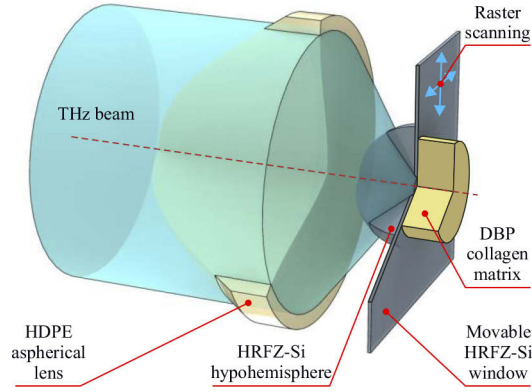


**Fig. 6.** A scheme of the THz beam focusing by an original solid immersion lens, that was developed in Refs. [51–54], operates in the continuous-wave reflection mode, and comprises the HDPE aspherical singlet, the HRFZ-Si hypohemisphere and the movable HRFZ-Si window with a DBP collagen matrix at the shadow side.

SIM system detects only the THz-wave intensity (power) and no information about its phase is available, we are able to estimate only the real dielectric permittivity  $\varepsilon'$ , while its imaginary part  $\varepsilon''$  is neglected.

At each point of the object plane  $\mathbf{r}$ , dielectric permittivity  $\varepsilon'$  is estimated via minimization of the following error functional

$$\varepsilon' = \operatorname{argmin}_{\varepsilon'} [M_{\text{exp}} - M_{\text{th}}(\varepsilon')], \quad (12)$$

where  $M_{\text{exp}}$  and  $M_{\text{th}}$  are the theoretical and experimental transfer functions. The function  $M_{\text{exp}}$  is calculated based on the object  $I_{\text{exp}}^{\text{obj}}$  and reference  $I_{\text{exp}}^{\text{ref}}$  signals

$$M_{\text{exp}} = \frac{I_{\text{exp}}^{\text{obj}}}{I_{\text{exp}}^{\text{ref}}}, \quad (13)$$

that correspond to intensities of the THz wave scattered from an imaged object or some reference medium with an *a priori*-known permittivity  $\varepsilon'_{\text{ref}}$ , respectively. In this work, air with  $\varepsilon'_{\text{ref}} = 1.0$  is used as a reference medium. The function  $M_{\text{th}}$  is defined analytically

$$M_{\text{th}}(\varepsilon') = \frac{I_{\text{th}}(\varepsilon')}{I_{\text{th}}(\varepsilon'_{\text{ref}})} \quad (14)$$

where  $I_{\text{th}}$  is a theoretical model describing the reflected THz-wave intensity as a function of  $\varepsilon'$ .

By considering all peculiarities of the THz-wave reflection from a solid immersion lens, the model  $I_{\text{th}}$  is defined

$$I_{\text{th}}(\varepsilon') = \frac{1}{2} |E^s(\varepsilon')|^2 + \frac{1}{2} |E^p(\varepsilon')|^2, \quad (15)$$

where the first and second terms correspond to the amplitudes of the *s*- and *p*-polarized waves, that exist within a wide THz beam aperture of our SIM system and are added incoherently. These amplitudes are comprised of the interfering ordinary-reflected and TIR waves, that exist below and above the critical angle of TIR effect – namely,  $\theta < \theta_{\text{TIR}}$  and  $\theta \geq \theta_{\text{TIR}}(\varepsilon')$ , correspondingly, where  $\theta_{\text{TIR}}(\varepsilon') = \arcsin(\sqrt{\varepsilon'}/n_{\text{Si}})$ . For the *s* and *p* polarizations, the total reflected wave amplitude

can be calculated by integration, over the aperture angle  $\theta$ , of the solid immersion lens reflectivity  $R^{s/p}(\theta, \varepsilon')$

$$E^{s/p}(\varepsilon') = E_0 \frac{\int_0^{\theta_{\max}} R^{s/p}(\theta, \varepsilon') \sin(\theta) d\theta}{\int_0^{\theta_{\max}} \sin(\theta) d\theta}. \quad (16)$$

Here,  $E_0$  is an amplitude of wave that radiates the HRFZ-Si hemisphere, and  $\theta_{\max} \simeq 40^\circ$  is the maximal aperture angle of our THz SIM system. The function  $R^{s/p}(\theta, \varepsilon')$  differs for the s and p polarizations and it automatically accounts for the ordinary reflection ( $\theta < \theta_{\text{TIR}}(\varepsilon')$ ) or TIR ( $\theta \geq \theta_{\text{TIR}}(\varepsilon')$ ) conditions at the Si/object interface for the particular combination of  $\varepsilon'$  and  $\theta$ . Moreover, it accounts for the multiple THz-wave reflections (standing waves) inside the HRFZ-Si hemisphere.

For the infinite coherence length of our backward-wave oscillator, the function  $R^{s/p}$  has the form

$$R^{s/p}(\theta, \varepsilon') = r_{0\text{-Si}} + \frac{t_{0\text{-Si}} t_{\text{Si-0}} p_{\text{Si}}^2 r^{s/p}(\theta, \varepsilon')}{1 - p_{\text{Si}}^2 r_{\text{Si-0}} r^{s/p}(\theta, \varepsilon')}, \quad (17)$$

where  $r_{0\text{-Si}}$ ,  $r_{\text{Si-0}}$  and  $t_{0\text{-Si}}$ ,  $t_{\text{Si-0}}$  are the polarization-dependent Fresnel reflection and transmission coefficients (by field) at the normal incidence [24,44,57], corresponding to the air/Si and Si/air interfaces; while  $p_{\text{Si}}$  is a THz-wave phase delay in the HRFZ-Si hemisphere governed by the modified Bouguer–Lambert–Beer law [24,44,57]

$$p_{\text{Si}} = \exp\left(-i \frac{2\pi\nu}{c_0} n_{\text{Si}} (l_1 + l_2)\right). \quad (18)$$

Parameter  $r^{s/p}$  describes the object- and polarization-dependent Fresnel reflection (by field) at the Si/object interface. For the s and p polarization states,  $r^{s/p}$  has the form:

$$\begin{aligned} r_{\text{Si/obj}}^s(\theta, \varepsilon') &= \frac{k_{z,\text{Si}}(\theta) - k_{z,\text{obj}}(\theta, \varepsilon')}{k_{z,\text{Si}}(\theta) + k_{z,\text{obj}}(\theta, \varepsilon')}, \\ r_{\text{Si/obj}}^p(\theta, \varepsilon') &= \frac{\varepsilon' k_{z,\text{Si}}(\theta) - n_{\text{Si}}^2 k_{z,\text{obj}}(\theta, \varepsilon')}{\varepsilon' k_{z,\text{Si}}(\theta) + n_{\text{Si}}^2 k_{z,\text{obj}}(\theta, \varepsilon')}, \end{aligned} \quad (19)$$

that governs both the ordinary-reflected ( $\theta < \theta_{\text{TIR}}$ ) and TIR ( $\theta \geq \theta_{\text{TIR}}$ ) waves, where:

$$\begin{aligned} k_{z,\text{Si}}(\theta) &= \frac{2\pi\nu}{c_0} n_{\text{Si}} \cos(\theta), \\ k_{z,\text{obj}}(\theta, \varepsilon') &= \frac{2\pi\nu}{c_0} \sqrt{\varepsilon' - n_{\text{Si}}^2 \sin^2(\theta)}. \end{aligned} \quad (20)$$

The method described by Eqs. (12)–20 yields estimation of the dielectric permittivity distribution over the object plane  $\varepsilon'(\mathbf{r})$  at the THz SIM operation wavelength of  $\lambda = 500 \mu\text{m}$  ( $\nu \simeq 0.6 \text{ THz}$ ) based on the THz microscopic images  $I(\mathbf{r})$ . For more information on the quantitative THz SIM method, and its applications for tissue imaging, see Ref. [56].

### 3. Results

The aforementioned instruments and methods allow us to study comprehensively the water vapor adsorption by tissues involving the following measured parameters:

- adsorption time constant  $\tau$ , calculated based on the TPS data;
- qualitative number of adsorbed water molecules  $N$  (per unit volume), calculated based on the TPS data;

- adsorption-associated increment of the sample mass  $\Delta m$ , calculated based on the weighting measurement;
- contact angle  $\gamma$  and total energy  $\sigma$  calculated based on the recumbent drop method;
- data on tissue heterogeneity, represented as a dielectric permittivity distribution over the sample surface  $\varepsilon''(\mathbf{r})$  and calculated based on the THz SIM data.

Notice that, at least, 3–4 DBP collagen matrices of each type are studied by the described instruments and methods.

In Fig. 7(a), a nomogram compares the mean values and standard deviations ( $\pm\sigma$  confidential interval) for the adsorption time constant  $\tau$  and the qualitative number of adsorbed water molecules  $N$ , estimated based on the TPS data. Both parameters  $\tau$ ,  $N$  have overall similar values for the considered intact DBPs, and those cross-linked by GA and treated by plasma, along with a very high dispersion of the measured parameters within each tissue type. The typical adsorption time constant is  $\tau \approx 8\text{--}10$  min. In Fig. 7(b), mass increment  $\Delta m$  is presented for the studied DBPs, which is in the range of  $\Delta m \approx 1\text{--}3\%$  and appears to be somewhat higher for the intact scaffold, as compared to the treated ones. Such a different increase in the intact and treated DBPs mass agrees with earlier reported data, that also involved tissue weighting before and after the water uptake [58]. At the same time, the observed dispersion of weight measurements is much bigger than the mass increment. Thus, it is quite debatable to claim any statistical differences between the measured parameters of the water vapor adsorption by tissues.

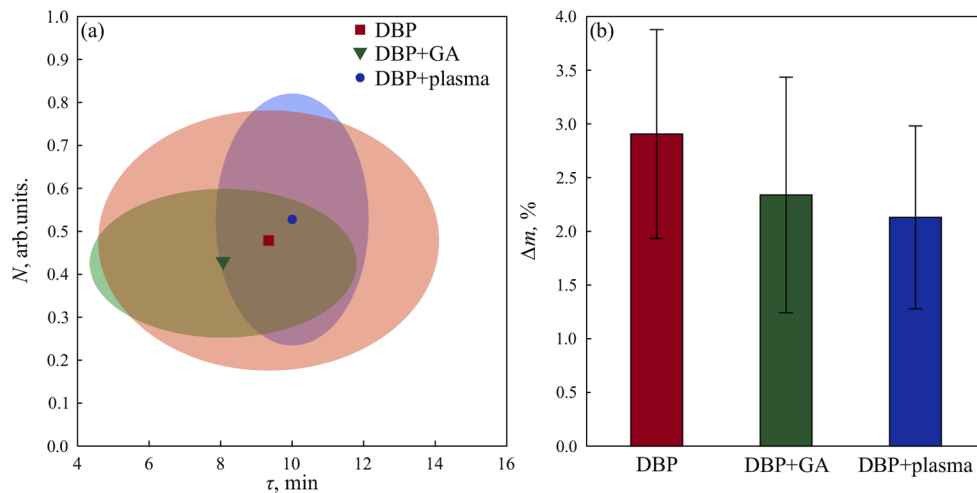
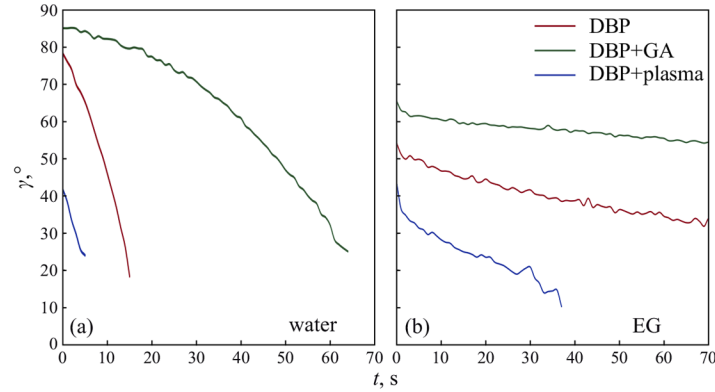


**Fig. 7.** Parameters of the water vapor adsorption calculated for the intact DBP collagen matrices and those cross-linked by GA and treated by plasma based on (a) the TPS data ( $\tau$ ,  $N$ ) and (b) the weight measurements ( $\Delta m$ ). At least 4 DBPs of each type were measured, which yields calculation of mean values and dispersions  $\sigma_\tau$ ,  $\sigma_N$ , and  $\sigma_{\Delta m}$  for the measured adsorption parameters  $\tau$ ,  $N$ , and  $\Delta m$ , correspondingly. Colored error areas in (a) and error bars in (b) represent the  $\pm\sigma_\tau$ ,  $\pm\sigma_N$ , and  $\pm\sigma_{\Delta m}$  confidential intervals, accounting for the natural variability of tissues.

Results of studying the surface properties of various DBPs by the recumbent drop method are shown in Fig. 8, with the calculated contact angle of wettability  $\gamma$  and the total surface energy  $\sigma$ . Despite all DBPs are hydrophilic, they show different water absorption kinetics. Intact DBPs absorb water for 15 sec. The GA-cross-linked samples (DBP+GA) have the highest contact angle, with water absorption duration of  $>1$  min. The plasma-treated samples (DBP+plasma)

demonstrate superhydrophilic properties – namely, for these samples, the contact angle at the initial point is 2 times lower than that of the intact DBPs, while water absorption by this material occurs 3 times faster. Similar trends are observed when using an organic solvent EG.



DBP samples	Contact angle $\gamma, ^\circ$ , (water/EG) at initial point	Surface energy and its components, mJ/m <sup>2</sup>		
		Polar, $\sigma^p$	Dispersion, $\sigma^d$	Energy, $\sigma^p + \sigma^d = \sigma$
DBP	(76±2)/(56±2)	9.5±1.5	19±2	28.5±2.5
DBP+GA	(88±3)/(65±2)	8±1	15±3	23±3
DBP+plasma	(45±3)/(43±2)	66±2	1.5±2	67.5±4

**Fig. 8.** Parameters of the contact angles of wettability calculated for the intact DBP collagen matrices and those cross-linked by GA and treated by plasma based on recumbent drop method in (a) water and (b) EG solution. At least 3 DBPs of each type were measured. Table represents values of DBPs contact angles at initial point and free energy of the sample surface. The spreads in Tab. show a  $\pm\sigma$  confidence interval.

Thus, DBP treatment somewhat affects the surface energy. Plasma treatment leads to an increase in the total surface energy due to the polar component  $\sigma^p$ . In this case, an increase in the polarity and hydrophilicity of the material is probably associated with the functionalization of its surface. On the contrary, cross-linking with GA provides a decrease in surface energy and a predominance of the dispersion component  $\sigma^d$ . Such changes are associated with the ordering and condensation of biological tissue fibers in the cross-linking process, which might somehow complicate the water absorption.

In this way, we demonstrate that treatment of the DBP collagen matrices by GA and plasma not only changes their mechanical and chemical performance, but also somewhat impact their interaction with water. At the same time, the observed effects of such treatments appeared to be quite small and, in certain cases, negligible as compared to the natural variability of the tissue properties. In our opinion, the measured data are quite important for further optimization of the scaffolds' preparation and treatment technologies in the tissue engineering and regenerative medicine.

The observed variability of the measured parameters is usual for the endogenous properties of biological tissues. In fact, it was earlier reported in a number of tissue studies involving different modalities of the sub-wavelength-resolution THz imaging; for example, see Refs. [6,19,51–54,56]. To confirm the hypothesis, in this work, THz SIM setup is applied for imaging of DBP samples, either in dehydrated form, or after their exposure to the  $80 \pm 5\%$  water vapor. In Fig. 9, sub-wavelength-resolution THz images of DBPs are shown in forms of the back-scattered THz-field intensity  $I(\mathbf{r})$ , the estimated dielectric permittivity distribution over the tissue area



$\varepsilon'(\mathbf{r})$ , and the image histograms  $p(\varepsilon')$ . Some fluctuations of the measured  $\varepsilon'$  can be attributed to raw sample surface and incomplete contact between the sample and the HRFZ-Si window, that leads to formation of air gaps between them and, thus, to some underestimations of  $\varepsilon'(\varepsilon')$ , as especially notable in Figs. 9(a),(b) and (m),(n). Nevertheless, the THz imaging data revealed strong fluctuations of the DBP optical properties over the sample aperture, as well as some predictable enhancement of the sample dielectric permittivity after its exposure to water vapor.

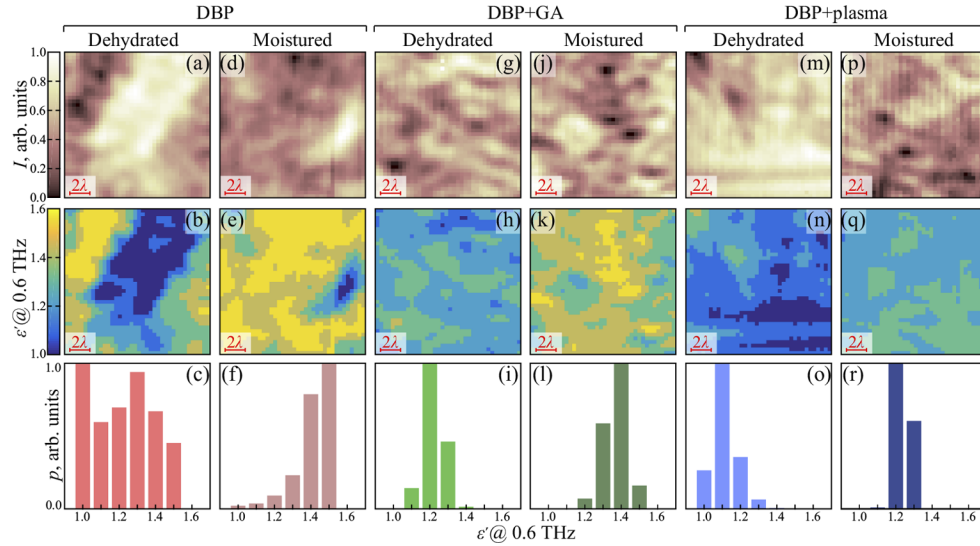


**Fig. 9.** THz SIM imaging, at  $\lambda = 500 \mu\text{m}$  ( $\nu \approx 0.6 \text{ THz}$ ), of the intact DBP collagen matrices and those cross-linked by GA and treated by plasma. The tissues were, first, dehydrated in vacuum for 1 hour and, then, moistured at the relative humidity of  $80 \pm 5\%$  for 1 hour. (a)–(c), (d)–(f) Measured THz images  $I(\mathbf{r})$ , estimated THz dielectric permittivity distributions  $\varepsilon'(\mathbf{r})$ , and calculated image histograms  $p(\varepsilon')$  for the dehydrated and moistured intact DBPs. (g)–(r) Equal data for the GA- and plasma-treated DBPs.

#### 4. Discussions

Tissue engineering offers a wide variety of biodegradable scaffolds that, in combination with cells and / or bioactive molecules (growth factors, cytokines, hormones, antibiotics, etc.), can replace damaged tissues of a living organism [59,60]. Currently, one of the most accessible and widespread source of cellular matrices is bovine pericardium that primarily consists of collagen type I [58,61]. Potential advantage of modifying such materials is the standardization of their manufacturing technology. Due to the controlled influence on the properties of matrices, it is possible to create structures with a constant composition, reproducible architectonics and specified physicochemical characteristics (hydrophilicity, porosity, etc.). The ability to customize such parameters opens up prospects for the creation of personalized implants, taking into account the anatomical and physiological characteristics of a particular patient [62].

Plasma treatment is a simple and scalable method for modifying the surface of biomaterials to increase their hydrophilicity [63,64]. Numerous studies have shown that cells cultured on structures treated with plasma exhibit better adhesion to the matrix surface [65,66]. Crosslinking with GA is a method for modifying biomaterials based on mammalian tissues. Chemical structuring increases proteolytic resistance and also reduces the immunogenicity of biological tissue by masking foreign antigens. However, the integration of such structures into the recipient's

body is complicated due to the acquired cytotoxicity, compaction of the material and the risk of calcification in the long-term postoperative period [67].

Quality control and safety monitoring must be performed throughout the entire manufacturing process to ensure the reliability and effectiveness of the implants. The water-absorbing properties are also an important indicator that needs to be monitored [1]. Reflecting the interactions of the cell with the scaffold, they determine such key parameters of implant integration as the rate of hydrolytic degradation, the degree of cell adhesion, transport of nutrients, etc. [1].

Water absorption can be investigated by various methods. For instance, Raman spectroscopy is vigorously explored as an analytical method for studying biomaterials, which allows obtaining high-resolution information on the biochemical composition and structure by creating spectral images [68]. However, the sensitivity of Raman spectroscopy and imaging to the tissue water in scaffolds is still to be examined. Coulometry is one of the electrochemical methods of analysis based on the measurement of the electric charge consumed in the electrolytic reduction or oxidation of a substance [69]. The disadvantages of this method are its time-consuming character, as well as partial current consumption for the passage of an uninteresting side reaction. Gravimetry is a method of quantitative chemical analysis based on the accurate measurement of the mass of a substance [70], which also possesses few drawbacks from the viewpoints of assessment of the water absorption properties: water can evaporate during the study, which reduces the accuracy of the results; gravimetry is quite laborious and takes more time compared to other methods.

Among other methods, THz technology holds strong potential in diagnosis of tissues and living cells, thanks to a low energy of THz quanta and high sensitivity of THz waves to the content and state of tissue water. THz spectroscopy and imaging are accurate and fast enough, and provide high-to-moderate spatial resolution, which makes it possible to consider THz technologies as a method of express diagnostics of biomaterials for tissue engineering and regenerative medicine [71]. Capabilities of THz technology for accessing the water content in decellularized biological tissues were comprehensively considered, for the first time, using both a common TPS method and a unique sub-wavelength-resolution THz-SIM system. Indeed, THz technology offers novel diagnostic capabilities in fabrication and treatment of scaffolds, aimed at solving challenging problems of tissue engineering and regenerative medicine.

Also, THz systems can be useful in other branches of regenerative medicine, including diagnostic applications in the tissue spheroid and bioprinting technologies. While pilot THz measurements of tissue spheroids were performed in Ref. [51], we still can only imagine possible diagnostic applications of THz technology in this rapidly-developing area of modern biomedicine. Indeed, there are prerequisite for the THz monitoring of intercellular matrix development, necrosis and other pathological tissue states in separate tissue spheroids, or in their agglomerates and related tissue constructs [5,6,19,20,28–30,34]. However, capabilities of THz technology in this area of regenerative medicine are still to be examined, which we postponed to our future studies.

## 5. Conclusion

In this paper, TPS and THz-SIM imaging, aided by common weight measurements and recumbent drop method, were used to study the water vapor adsorption by the DBP collagen matrices. Both intact DBPs and those cross-linked by GA and treated by plasma (aimed at managing the mechanical properties of tissues) were measured. Changes in the tissue THz dielectric response and mass were studied during their exposure to water vapor. Adsorption time constants, tissue mass increment, and these parameters dispersion were estimated based on the measured data. With an increasing adsorption time, changes in the DBPs' response at THz frequencies have an exponential character, with the typical adsorption time constant of 8–10 min, the transient process saturation at 30 min, and the tissue mass increase by 1–3%. After additional measurements of the contact angles of wettability and the total surface energy of the considered tissues, we

concluded that treatments of DBPs by GA or plasma somewhat impact their interaction with water. However, the observed effects are small as compared to the natural variability of the tissue properties. Finally, the THz microscopy justified such a strong heterogeneity of tissues at the THz-wavelength scale and confirmed the abovementioned variability of the tissue properties.

**Funding.** Russian Science Foundation (18-15-00401).

**Acknowledgements.** This work was supported by the Russian Science Foundation (RSF), Project # 18-15-00401. Special gratitude for help is expressed to Kuryanova A.S., the junior researcher of the World-Class Research Center "Digital Biodesign and Personalized Healthcare", Moscow, Russia.

**Disclosures.** The authors declare no conflict of interest.

**Data availability.** Data underlying the results presented in this paper are not publicly available at this time but may be obtained from the authors upon reasonable request.

## References

1. T. L. do Amaral Montanheiro, L. S. Montagna, V. Patrulea, O. Jordan, G. Borchard, R. G. Ribas, T. M. B. Campos, G. P. Thim, and A. P. Lemes, "Enhanced water uptake of PHBV scaffolds with functionalized cellulose nanocrystals," *Polym. Test.* **79**, 106079 (2019).
2. A. Maslinda, M. A. Majid, M. Ridzuan, M. Afendi, and A. Gibson, "Effect of water absorption on the mechanical properties of hybrid interwoven cellulosic-cellulosic fibre reinforced epoxy composites," *Compos. Struct.* **167**, 227–237 (2017).
3. Y. Zhang, J. Zhao, G. Yang, Y. Zhou, W. Gao, G. Wu, X. Li, C. Mao, T. Sheng, and M. Zhou, "Mechanical properties and degradation of drug eluted bioresorbable vascular scaffolds prepared by three-dimensional printing technology," *J. Biomater. Sci., Polym. Ed.* **30**(7), 547–560 (2019).
4. E. Pickwell and V. Wallace, "Biomedical applications of terahertz technology," *J. Phys. D: Appl. Phys.* **39**(17), R301–R310 (2006).
5. X. Yang, X. Zhao, K. Yang, Y. Liu, Y. Liu, W. Fu, and Y. Luo, "Biomedical applications of terahertz spectroscopy and imaging," *Trends Biotechnol.* **34**(10), 810–824 (2016).
6. O. Smolyanskaya, N. Chernomyrdin, A. Konovko, K. Zaytsev, I. Ozheredov, O. Cherkasova, M. Nazarov, J.-P. Guillet, S. Kozlov, Y. Kistenev, J.-L. Coutaz, P. Mounaix, V. Vaks, J.-H. Son, H. Cheon, V. Wallace, Y. Feldman, I. Popov, A. Yaroslavsky, A. Shkurinov, and V. Tuchin, "Terahertz biophotonics as a tool for studies of dielectric and spectral properties of biological tissues and liquids," *Prog. Quantum Electron.* **62**, 1–77 (2018).
7. A. Nikitkina, P. Bikmulina, E. Gafarova, N. Kosheleva, Y. Efremov, E. Bezrukov, D. Butnaru, I. Dolganova, N. Chernomyrdin, O. Cherkasova, A. Gavdush, and P. Timashev, "Terahertz radiation and the skin: a review," *J. Biomed. Opt.* **26**(04), 043005 (2021).
8. A. Gavdush, N. Chernomyrdin, G. Komandin, I. Dolganova, P. Nikitin, G. Musina, G. Katyba, A. Kucheryavenko, I. Reshetov, A. Potapov, V. Tuchin, and K. Zaytsev, "Terahertz dielectric spectroscopy of human brain gliomas and intact tissues ex vivo: double-Debye and double-overdamped-oscillator models of dielectric response," *Biomed. Opt. Express* **12**(1), 69–83 (2021).
9. K. Ahi, N. Jessurun, M.-P. Hosseini, and N. Asadizanjani, "Survey of terahertz photonics and biophotonics," *Opt. Eng.* **59**(06), 1 (2020).
10. H. Guerboukha, K. Nallappan, and M. Skorobogatiy, "Toward real-time terahertz imaging," *Adv. Opt. Photonics* **10**(4), 843–938 (2018).
11. A. Yachmenev, D. Lavrukhin, I. Glinskiy, N. Zenchenko, Y. Goncharov, I. Spektor, R. Khabibullin, T. Otsuji, and D. Ponomarev, "Metallic and dielectric metasurfaces in photoconductive terahertz devices: a review," *Opt. Eng.* **59**(06), 1 (2019).
12. M. Manjappa and R. Singh, "Materials for terahertz optical science and technology," *Adv. Opt. Mater.* **8**(3), 1901984 (2020).
13. A. E. Yachmenev, S. S. Pushkarev, R. R. Reznik, R. A. Khabibullin, and D. S. Ponomarev, "Arsenides-and related III-V materials-based multilayered structures for terahertz applications: Various designs and growth technology," *Prog. Cryst. Growth Charact. Mater.* **66**(2), 100485 (2020).
14. A. Gavdush, N. Chernomyrdin, D. Lavrukhin, Y. Cao, G. Komandin, I. Spektor, A. Perov, I. Dolganova, G. Katyba, V. Kurlov, D. Ponomarev, M. Skorobogatiy, I. Reshetov, and K. Zaytsev, "Proof of concept for continuously-tunable terahertz bandpass filter based on a gradient metal-hole array," *Opt. Express* **28**(18), 26228–26238 (2020).
15. K. I. Zaytsev, G. M. Katyba, N. V. Chernomyrdin, I. N. Dolganova, A. S. Kucheryavenko, A. N. Rossolenko, V. V. Tuchin, V. N. Kurlov, and M. Skorobogatiy, "Overcoming the Abbe diffraction limit using a bundle of metal-coated high-refractive-index sapphire optical fibers," *Adv. Opt. Mater.* **8**(18), 2000307 (2020).
16. G. Katyba, K. Zaytsev, I. Dolganova, N. Chernomyrdin, V. Ulitko, S. Rossolenko, I. Shikunova, and V. Kurlov, "Sapphire waveguides and fibers for terahertz applications," *Prog. Cryst. Growth Charact. Mater.* **67**(3), 100523 (2021).

17. V. Ulitko, A. Zotov, A. Gavdush, G. Katyba, G. Komandin, I. Spektor, I. Shmytko, G. Emelchenko, I. Dolganova, M. Skorobogatiy, V. Kurlov, V. Masalov, and K. Zaytsev, "Nanoporous SiO<sub>2</sub> based on annealed artificial opals as a favorable material platform of terahertz optics," *Opt. Mater. Express* **10**(9), 2100–2113 (2020).
18. V. Ulitko, G. Katyba, V. Zhelnov, I. Shmytko, G. Emelchenko, I. Spektor, V. Masalov, V. Kurlov, K. Zaytsev, and M. Skorobogatiy, "Opal-based terahertz optical elements fabricated by self-assembly of porous SiO<sub>2</sub> nanoparticles," *Opt. Express* **29**(9), 13764–13777 (2021).
19. K. Zaytsev, I. Dolganova, N. Chernomyrdin, G. Katyba, A. Gavdush, O. Cherkasova, G. Komandin, M. Shchedrina, A. Khodan, D. Ponomarev, I. Reshetov, V. Karasik, M. Skorobogatiy, V. Kurlov, and V. Tuchin, "The progress and perspectives of terahertz technology for diagnosis of neoplasms: a review," *J. Opt.* **22**(1), 013001 (2020).
20. G. Musina, P. Nikitin, N. Chernomyrdin, I. Dolganova, A. Gavdush, G. Komandin, D. Ponomarev, A. Potapov, I. Reshetov, V. Tuchin, and K. Zaytsev, "Prospects of terahertz technology in diagnosis of human brain tumors – a review," *J. Biomed. Photonics Eng.* **6**(2), 3375 (2020).
21. R. Woodward, V. Wallace, D. Arnone, E. Linfield, and M. Pepper, "Terahertz pulsed imaging of skin cancer in the time and frequency domain," *J. Biol. Phys.* **29**(2/3), 257–259 (2003).
22. V. Wallace, A. Fitzgerald, S. Shankar, N. Flanagan, R. Pye, J. Cluff, and D. Arnone, "Terahertz pulsed imaging of basal cell carcinoma ex vivo and in vivo," *Br. J. Dermatol.* **151**(2), 424–432 (2004).
23. P. Ashworth, E. Pickwell-MacPherson, E. Provenzano, S. Pinder, A. Purushotham, M. Pepper, and V. Wallace, "Terahertz pulsed spectroscopy of freshly excised human breast cancer," *Opt. Express* **17**(15), 12444–12454 (2009).
24. A. Gavdush, N. Chernomyrdin, K. Malakhov, S.-I. Beshplav, I. Dolganova, A. Kosyrkova, P. Nikitin, G. Musina, G. Katyba, I. Reshetov, O. Cherkasova, G. Komandin, V. Karasik, A. Potapov, V. Tuchin, and K. Zaytsev, "Terahertz spectroscopy of gelatin-embedded human brain gliomas of different grades: a road toward intraoperative THz diagnosis," *J. Biomed. Opt.* **24**(02), 1 (2019).
25. M. Konnikova, O. Cherkasova, M. Nazarov, D. Vrazhnov, Y. Kistenev, S. Titov, E. Kopeikina, S. Shevchenko, and A. Shkurinov, "Malignant and benign thyroid nodule differentiation through the analysis of blood plasma with terahertz spectroscopy," *Biomed. Opt. Express* **12**(2), 1020–1035 (2021).
26. M. Borovkova, M. Khodzitsky, P. Demchenko, O. Cherkasova, A. Popov, and I. Meglinski, "Terahertz time-domain spectroscopy for non-invasive assessment of water content in biological samples," *Biomed. Opt. Express* **9**(5), 2266–2276 (2018).
27. A. Shchepetilnikov, A. Zarezin, V. Muravev, P. Gusikhin, and I. Kukushkin, "Quantitative analysis of water content and distribution in plants using terahertz imaging," *Opt. Eng.* **59**(06), 1 (2020).
28. J. Shi, Y. Wang, T. Chen, D. Xu, H. Zhao, L. Chen, C. Yan, L. Tang, Y. He, H. Feng, and J. Yao, "Automatic evaluation of traumatic brain injury based on terahertz imaging with machine learning," *Opt. Express* **26**(5), 6371–6381 (2018).
29. Y. Cao, P. Huang, J. Chen, W. Ge, D. Hou, and G. Zhang, "Qualitative and quantitative detection of liver injury with terahertz time-domain spectroscopy," *Biomed. Opt. Express* **11**(2), 982–993 (2020).
30. M. Arbab, D. Winebrenner, T. Dickey, A. Chen, M. Klein, and P. Mourad, "Terahertz spectroscopy for the assessment of burn injuries in vivo," *J. Biomed. Opt.* **18**(7), 077004 (2013).
31. G. Hernandez-Cardoso, S. Rojas-Landeros, M. Alfaro-Gomez, A. Hernandez-Serrano, I. Salas-Gutierrez, E. Lemus-Bedolla, A. Castillo-Guzman, H. Lopez-Lemus, and E. Castro-Camus, "Terahertz imaging for early screening of diabetic foot syndrome: A proof of concept," *Sci. Rep.* **7**(1), 42124 (2017).
32. O. Cherkasova, M. Nazarov, and A. Shkurinov, "Noninvasive blood glucose monitoring in the terahertz frequency range," *Opt. Quantum Electron.* **48**(3), 217 (2016).
33. O. Smolyanskaya, I. Schelkanova, M. Kulya, E. Odlyanitskiy, I. Goryachev, A. Tcypkin, Y. Grachev, Y. Toropova, and V. Tuchin, "Glycerol dehydration of native and diabetic animal tissues studied by THz-TDS and NMR methods," *Biomed. Opt. Express* **9**(3), 1198–1215 (2018).
34. J. Wang, H. Lindley-Hatcher, K. Liu, and E. Pickwell-MacPherson, "Evaluation of transdermal drug delivery using terahertz pulsed imaging," *Biomed. Opt. Express* **11**(8), 4484–4490 (2020).
35. K. Motovilov, M. Savinov, E. Zhukova, A. Pronin, Z. Gagkaeva, V. Grinenko, K. Sidoruk, T. Voeikova, P. Y. Barzilovich, and A. Grebenko, "Observation of dielectric universalities in albumin, cytochrome C and *Shewanella oneidensis* MR-1 extracellular matrix," *Sci. Rep.* **7**(1), 15731 (2017).
36. Z. Gagkaeva, E. Zhukova, V. Grinenko, A. Grebenko, K. Sidoruk, T. Voeikova, M. Dressel, and B. Gorshunov, "Terahertz-infrared spectroscopy of *Shewanella oneidensis* mr-1 extracellular matrix," *J. Biol. Phys.* **44**(3), 401–417 (2018).
37. E. Marzec, J. Olszewski, J. Kaczmarczyk, M. Richter, T. Trzeciak, K. Nowocień, R. Malak, and W. Samborski, "Dielectric study of interaction of water with normal and osteoarthritis femoral condyle cartilage," *Bioelectrochemistry* **110**, 32–40 (2016).
38. J. Brzeziński, G. Oszkiniś, and E. Marzec, "Dielectric relaxation of a protein–water system in atherosclerotic artery wall," *Med. Biol. Eng. Comput.* **45**(6), 525–529 (2007).
39. R. I. Stantchev, J. C. Mansfield, R. S. Edginton, P. Hobson, F. Palombo, and E. Hendry, "Subwavelength hyperspectral THz studies of articular cartilage," *Sci. Rep.* **8**(1), 6924 (2018).
40. G. Komandin, A. Gavdush, Y. G. Goncharov, O. Porodinkov, V. Nozdrin, S. Chuchupal, and I. Spektor, "Electrodynamical characteristics of  $\alpha$ -lactose monohydrate in the terahertz range," *Opt. Spectrosc.* **126**(5), 514–522 (2019).



41. G. Komandin, V. Anzin, V. Ulitko, A. Gavdush, A. Mukhin, Y. Goncharov, O. Porodinkov, and I. Spektor, "Optical cryostat with sample rotating unit for polarization-sensitive terahertz and infrared spectroscopy," *Opt. Eng.* **59**(06), 1 (2019).
42. D. Lavrukhin, A. Yachmenev, A. Pavlov, R. Khabibullin, Y. Goncharov, I. Spektor, G. Komandin, S. Yurchenko, N. Chernomyrdin, K. Zaytsev, and D. Ponomarev, "Shaping the spectrum of terahertz photoconductive antenna by frequency-dependent impedance modulation," *Semicond. Sci. Technol.* **34**(3), 034005 (2019).
43. G. Musina, I. Dolganova, N. Chernomyrdin, A. Gavdush, V. Ulitko, O. Cherkasova, D. Tuchina, P. Nikitin, A. Alekseeva, N. Bal, G. Komandin, V. Kurlov, V. Tuchin, and K. Zaytsev, "Optimal hyperosmotic agents for tissue immersion optical clearing in terahertz biophotonics," *J. Biophotonics* **13**(12), e202000297 (2020).
44. K. Zaytsev, A. Gavdush, V. Karasik, V. Alekhnovich, P. Nosov, V. Lazarev, I. Reshetov, and S. Yurchenko, "Accuracy of sample material parameters reconstruction using terahertz pulsed spectroscopy," *J. Appl. Phys.* **115**(19), 193105 (2014).
45. G. Komandin, V. Nozdrin, A. Gavdush, A. Pronin, O. Porodinkov, I. Spektor, V. Sigaev, A. Mikhailov, G. Shakhgildyan, V. Ulitko, and D. Abdullaev, "Effect of moisture adsorption on the broadband dielectric response of SiO<sub>2</sub>-based nanoporous glass," *J. Appl. Phys.* **126**(22), 224303 (2019).
46. L. Oliveira, M. Carvalho, E. Nogueira, and V. Tuchin, "Diffusion characteristics of ethylene glycol in skeletal muscle," *J. Biomed. Opt.* **20**(5), 051019 (2014).
47. M. Al-Sharabi, D. Markl, V. Vivacqua, P. Bawuah, N. MacLean, M. Bentley, A. P. York, M. Marigo, K. Huang, and J. A. Zeidler, "Terahertz pulsed imaging as a new method for investigating the liquid transport kinetics of  $\alpha$ -alumina powder compacts," *Chem. Eng. Res. Des.* **165**, 386–397 (2021).
48. H. Lin, B. Russell, P. Bawuah, and J. Zeidler, "Sensing water absorption in hygrothermally aged epoxies with terahertz time-domain spectroscopy," *Anal. Chem.* **93**(4), 2449–2455 (2021).
49. O. Cherkasova, M. Nazarov, M. Konnikova, and A. Shkurinov, "THz spectroscopy of bound water in glucose: direct measurements from crystalline to dissolved state," *J. Infrared, Millimeter, Terahertz Waves* **41**(9), 1057–1068 (2020).
50. E. Buixaderas, S. Kamba, and J. Petzelt, "Lattice dynamics and central-mode phenomena in the dielectric response of ferroelectrics and related materials," *Ferroelectrics* **308**(1), 131–192 (2004).
51. N. Chernomyrdin, A. Kucheryavenko, G. Kolontaeva, G. Katyba, I. Dolganova, P. Karalkin, D. Ponomarev, V. Kurlov, I. Reshetov, M. Skorobogatiy, V. Tuchin, and K. Zaytsev, "Reflection-mode continuous-wave 0.15- $\lambda$ -resolution terahertz solid immersion microscopy of soft biological tissues," *Appl. Phys. Lett.* **113**(11), 111102 (2018).
52. N. Chernomyrdin, A. Kucheryavenko, E. Rims kaya, I. Dolganova, V. Zhelnov, P. Karalkin, A. Gryadunova, I. Reshetov, D. Lavrukhin, D. Ponomarev, V. Karasik, and K. Zaytsev, "Terahertz microscope based on solid immersion effect for imaging of biological tissues," *Opt. Spectrosc.* **126**(5), 560–567 (2019).
53. N. Chernomyrdin, V. Zhelnov, A. Kucheryavenko, I. Dolganova, G. Katyba, V. Karasik, I. Reshetov, and K. Zaytsev, "Numerical analysis and experimental study of terahertz solid immersion microscopy," *Opt. Eng.* **59**(06), 1 (2019).
54. V. Zhelnov, K. Zaytsev, A. Kucheryavenko, G. Katyba, I. Dolganova, D. Ponomarev, V. Kurlov, M. Skorobogatiy, and N. Chernomyrdin, "Object-dependent spatial resolution of the reflection-mode terahertz solid immersion microscopy," *Opt. Express* **29**(3), 3553–3566 (2021).
55. D. Grischkowsky, S. Keiding, M. van Exter, and C. Fattinger, "Far-infrared time-domain spectroscopy with terahertz beams of dielectrics and semiconductors," *J. Opt. Soc. Am. B* **7**(10), 2006–2015 (1990).
56. A. Kucheryavenko, N. Chernomyrdin, A. Gavdush, A. Alekseeva, P. Nikitin, I. Dolganova, P. Karalkin, A. Khalansky, I. Spektor, M. Skorobogatiy, V. Tuchin, and K. Zaytsev, "Terahertz dielectric spectroscopy and solid immersion microscopy of ex vivo glioma model 101.8: brain tissue heterogeneity," *Biomed. Opt. Express* **12**(11), 69–83 (2021).
57. B. Giuliano, A. Gavdush, B. Muller, K. Zaytsev, T. Grassi, A. Ivlev, M. Palumbo, G. Baratta, C. Scire, G. Komandin, S. Yurchenko, and P. Caselli, "Broadband spectroscopy of astrophysical ice analogues – I. direct measurement of the complex refractive index of CO ice using terahertz time-domain spectroscopy," *Astron. & Astrophys.* **629**, A112 (2019).
58. E. A. Grebenik, L. P. Istranov, E. V. Istranova, S. N. Churbanov, B. S. Shavkuta, R. I. Dmitriev, N. N. Veryasova, S. L. Kotova, A. V. Kurkov, and A. B. Shekhter, "Chemical cross-linking of xenopericardial biomeses: A bottom-up study of structural and functional correlations," *Xenotransplantation* **26**(3), e12506 (2019).
59. M. P. Nikolova and M. S. Chavali, "Recent advances in biomaterials for 3D scaffolds: a review," *Bioact. Mater.* **4**, 271–292 (2019).
60. E. R. Gafarova, E. A. Grebenik, A. E. Lazhko, A. A. Frolova, A. S. Kuryanova, A. V. Kurkov, I. A. Bazhanov, B. S. Kapomba, N. V. Kosheleva, and I. A. Novikov, "Evaluation of supercritical CO<sub>2</sub>-assisted protocols in a model of ovine aortic root decellularization," *Molecules* **25**(17), 3923 (2020).
61. E. A. Grebenik, E. R. Gafarova, L. P. Istranov, E. V. Istranova, X. Ma, J. Xu, W. Guo, A. Atala, and P. S. Timashev, "Mammalian pericardium-based bioprosthetic materials in xenotransplantation and tissue engineering," *Biotechnol. J.* **15**(8), 1900334 (2020).
62. J. Xing, Y. Lu, Y. Cui, X. Zhu, F. Luo, Z. Xie, X. Wu, M. Deng, J. Xu, and T. Hou, "A standardized and quality-controllable protocol of constructing individual tissue-engineered grafts applicable to treating large bone defects," *Tissue Eng., Part C* **25**(3), 137–147 (2019).
63. L. Minati, C. Migliaresi, L. Lunelli, G. Viero, M. Dalla Serra, and G. Speranza, "Plasma assisted surface treatments of biomaterials," *Biophys. Chem.* **229**, 151–164 (2017).



64. T. S. Demina, M. G. Drozdova, M. Y. Yablokov, A. I. Gaidar, A. B. Gilman, D. S. Zaytseva-Zotova, E. A. Markvicheva, T. A. Akopova, and A. N. Zelenetskii, "DC discharge plasma modification of chitosan films: an effect of chitosan chemical structure," *Plasma Process. Polym.* **12**(8), 710–718 (2015).
65. D. Ujino, H. Nishizaki, S. Higuchi, S. Komasa, and J. Okazaki, "Effect of plasma treatment of titanium surface on biocompatibility," *Appl. Sci.* **9**(11), 2257 (2019).
66. P. Das, N. Ojah, R. Kandimalla, K. Mohan, D. Gogoi, S. K. Dolui, and A. J. Choudhury, "Surface modification of electrospun pva/chitosan nanofibers by dielectric barrier discharge plasma at atmospheric pressure and studies of their mechanical properties and biocompatibility," *Int. J. Biol. Macromol.* **114**, 1026–1032 (2018).
67. G. M. Gunning and B. P. Murphy, "The effects of decellularization and cross-linking techniques on the fatigue life and calcification of mitral valve chordae tendineae," *J. Mech. Behav. Biomed. Mater.* **57**, 321–333 (2016).
68. H. J. Butler, L. Ashton, B. Bird, G. Cinque, K. Curtis, J. Dorney, K. Esmonde-White, N. J. Fullwood, B. Gardner, and P. L. Martin-Hirsch, "Using Raman spectroscopy to characterize biological materials," *Nat. Protoc.* **11**(4), 664–687 (2016).
69. M. B. Ayoub, R. Aro, E. Georgin, J. F. Rochas, and P. Sabouroux, "Quantification of free and bound water in selected materials using dielectric and thermo-coulometric measurement methods," *J. Phys. Commun.* **2**(3), 035040 (2018).
70. A. Sendra-García, M. A. Martínez-Gómez, A. Albert-Marí, N. V. Jiménez-Torres, and M. Climente-Martí, "Quantitative and qualitative control of antineoplastic preparations: Gravimetry versus HPLC," *J. Oncol. Pharm. Pract.* **25**(5), 1204–1216 (2019).
71. J. Li, Y. Yao, L. Jiang, S. Li, Z. Yi, X. Chen, Z. Tian, and W. Zhang, "Time-domain terahertz optoacoustics: manipulable water sensing and dampening," *Adv. Photonics* **3**(02), 026003 (2021).